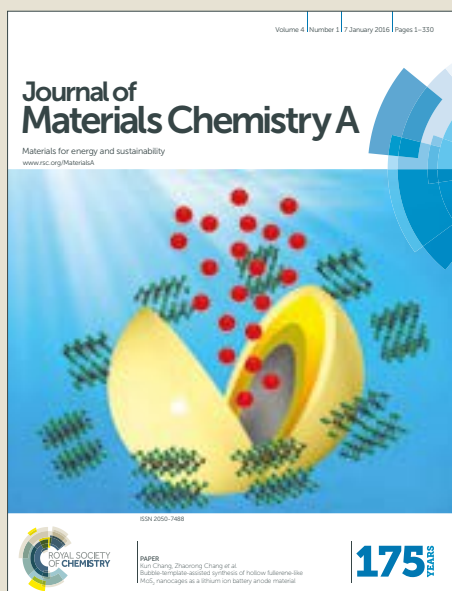


Journal of Materials Chemistry A

Accepted Manuscript



This article can be cited before page numbers have been issued, to do this please use: F. W. D. S. W. D. S. Lucas, H. Peng, S. Johnston, P. C. Dippo, S. Lany, L. H. Mascaro and A. Zakutayev, *J. Mater. Chem. A*, 2017, DOI: 10.1039/C7TA07012H.



This is an Accepted Manuscript, which has been through the Royal Society of Chemistry peer review process and has been accepted for publication.

Accepted Manuscripts are published online shortly after acceptance, before technical editing, formatting and proof reading. Using this free service, authors can make their results available to the community, in citable form, before we publish the edited article. We will replace this Accepted Manuscript with the edited and formatted Advance Article as soon as it is available.

You can find more information about Accepted Manuscripts in the [author guidelines](#).

Please note that technical editing may introduce minor changes to the text and/or graphics, which may alter content. The journal's standard [Terms & Conditions](#) and the ethical guidelines, outlined in our [author and reviewer resource centre](#), still apply. In no event shall the Royal Society of Chemistry be held responsible for any errors or omissions in this Accepted Manuscript or any consequences arising from the use of any information it contains.

Characterization of defects in copper antimony disulfide

Francisco Willian de Souza Lucas^{a,b}, Haowei Peng^a, Steve Johnston^a, Patricia C. Dippo^a,
Stephan Lany^a, Lucia H. Mascaro^b, Andriy Zakutayev^{a*}

^a National Renewable Energy Laboratory, Golden, CO 80401, USA.

^b Federal University of Sao Carlos, São Carlos, SP 13565-905, Brazil.

*Corresponding author, e-mail: andriy.zakutayev@nrel.gov

Abstract

Copper antimony disulfide (CuSbS₂) with chalcostibite structure is a promising photovoltaic (PV) absorber material with several excellent measured optoelectronic properties, such as solar matched band gap and tunable hole concentration. However, much less is known from experimental perspective about defects in CuSbS₂, even though the defects are critical for solar cell performance. Here, we explore the defect properties in CuSbS₂ thin film materials and photovoltaic devices using photoluminescence and capacitance-based spectroscopies, as well as first principles theoretical calculations. We measured three electrically and optically active acceptor defects in CuSbS₂, and assigned them to the copper vacancies, sulfur vacancies, and/or copper on antimony antisites by comparison with theoretical calculations. Their activation energies, concentrations, and capture cross sections have been determined and compared to other chalcogenide absorber materials. These fundamental parameters should enable more accurate simulations of CuSbS₂ PV devices, paving the way to the future improvements in CuSbS₂ solar cell efficiencies.

1. Introduction

Copper antimony sulfide (CuSbS_2), with the chalcocite crystal structure, is an emerging non-toxic and earth-abundant photovoltaic (PV) absorber material. It features an optical absorption coefficient larger than 10^5 cm^{-1} at 1.8 eV,¹⁻³ a slightly indirect band gap of 1.4–1.5 eV,¹⁻⁵ tunable hole concentrations in the range of 10^{16} – 10^{18} cm^{-3} , and a hole mobility of 0.1–1.0 cm^2/Vs in polycrystalline thin films.^{1,2} Despite these promising basic optoelectronic properties, there are few experimental studies of other PV-relevant properties related to defect concentration and carrier recombination. Better understanding of these properties is crucial for an enhanced efficiency of the CuSbS_2 thin-film solar cells.

The current highest efficiency of the CuSbS_2 thin-film solar cell is only 3.13%,⁴ (close to 1% from several other reports^{2,6,7}), comparable to the almost 5% efficiency of the isostructural CuSbSe_2 device.⁶ What are the limiting factors for these relatively low efficiencies? Some researchers argued that well-defined ohmic contacts could improve the CuSbS_2 device efficiency.² Others proposed the large band-offset between the absorber and the commonly used CdS contact layer as one of the limiting factors.^{6,7} Yet another group has shown, by calculating the defect formation enthalpies, that copper vacancies (V_{Cu}) are the defects that control the *p*-type conductivity in CuSbS_2 , and documented the calculated formation enthalpies of other possible defects.³ In this study, we provide the missing detailed experimental defect characterization for this material, and show how specific defects can limit the device performance beyond controlling the equilibrium hole concentration.

There are many advanced material- and device-characterization techniques to study the influence of defects on the performance of photovoltaic devices. For example, photoluminescence (PL) spectroscopy can be used to observe radiative transitions associated with defects in semiconductors.^{8,9} Combining the PL measurement with first-principles calculations further enables attributing the PL transitions to specific defects.¹⁰⁻¹⁴ PV-device

characterization techniques based on capacitance-voltage measurements are another set of powerful methods. Admittance spectroscopy (AS) provides insight into the energetic position and the density of states of the defects.⁸ Deep level transient spectroscopy (DLTS) enables quantification of the defects type (donor or acceptor), activation energies, defects concentrations, and capture cross-sections.¹⁵

Here, we investigate the defect properties in CuSbS₂ material from both experimental and computational perspectives of this material, as well as from experimental characterizations of CuSbS₂-based PV-devices. We prepared and characterized three types of CuSbS₂ material samples: as-deposited and annealed CuSbS₂ thin films on glass and molybdenum/soda-lime glass (Mo/SLG) substrates; CuSbS₂ micro-crystals grown on Mo/SLG substrate; and CuSbS₂ solar cell devices based on the annealed thin-film samples. Our study spans from *macroscopic* capacitance-based measurements of the defects present in the PV device, to *microscopic* evaluation of the radiative behavior of these defects by temperature- and power-dependent photoluminescence in thin films, and to *atomic-scale* defect identification by first-principles calculations. Combining the results from all of these techniques, we propose a model of defect levels within the band gap for CuSbS₂. We expect this new fundamental understanding of defect physics in CuSbS₂ to aid future improvements in efficiencies of the CuSbS₂-based solar cells.

2. Methods

CuSbS₂ films were deposited by the self-regulated growth approach,^{1,16} using the radio frequency (RF) magnetron co-sputtering of one 5-cm-diameter Cu₂S and two 5-cm-diameter Sb₂S₃ targets (99.999%) with a power of 40 W applied to each. The same chamber conditions were used to grow the Cu₂S/Mo/soda lime glass (SLG) precursor thin films, but only using the Cu₂S target. Deposition of the phase-pure stoichiometric CuSbS₂ films was performed in

3 mTorr of Argon (99.99%) in a 40L vacuum chamber with a base pressure of 10^{-7} Torr on a $5 \times 5 \text{ cm}^2$ Mo/SLG substrate. The resulting film thickness was in the range of 1.4-1.6 μm . More details of the CuSbS_2 thin film deposition process have been reported previously.¹

Thermal treatment (TT) was performed in a one-zone tube furnace under a N_2 atmosphere rich with Sb_2S_3 vapor at 455°C for 11h, following the previously reported optimized condition.¹⁷ The CuSbS_2 crystals supported on Mo/SLG films were grown by annealing a $\sim 500 \text{ nm}$ Cu_2S film under the condition of the aforementioned TT. For simplification, the microcrystals supported on Mo/SLG will be referred as “crystals” in the following text. Both the films and the crystals were subjected to a selective chemical etch for removal of Sb_2S_3 secondary phase that could be formed during thermal treatment, as described in our prior publication¹⁷. PV devices with the Mo/*p*- CuSbS_2 /*n*-CdS/*i*-ZnO/ZnO:Al/Al architecture were fabricated from annealed films (TT-11h) by chemical bath deposition of CdS, RF sputtering of intrinsic/conductive transparent *i*-ZnO/ZnO:Al, and an e-beam evaporation of aluminum grid, as described elsewhere.^{6,7,17,18}

Phase identification of the films and the crystals was performed by X-ray diffraction (XRD) (Bruker D8 Discover). The composition and thickness of the pre- and post-thermal treated films (pre-TT and TT-11h, respectively) were obtained by X-ray fluorescence (XRF) (Fischerscope[®] X-Ray XDV[®]-SDD, Helmut Fischer GmbH). The carrier concentration was evaluated by Hall effect measurements (Accent HL5500PC[®]) using van der Pauw resistance configuration at room temperature.

Photoluminescence (PL) experiments on films (as grown and annealed) and on crystals were performed in a helium closed-cycle cryostat, where excitation dependent PL experiments were taken at 4.25 K with laser powers from 0.1 to 16 mW. The temperature-dependent experiments were taken from 4.25 K to the room temperature (RT). A HeNe laser ($\lambda = 632.8 \text{ nm}$, or $E_g = 1.960 \text{ eV}$) was used for excitation, with a 5-second exposure time, 280-

μm slit, and a 695-nm-long pass filter. The PL spectra were collected by a spectrometer with a diffraction grating of 600 grooves/mm and a 1024x256 pixel charge coupled device (CCD). PL spectra were analyzed by fitting the measured spectra to Gaussian curves.

Admittance Spectroscopy (AS) and deep-level transient spectroscopy (DLTS) studies were performed on devices with the architecture of Mo/*p*-CuSbS₂/*n*-CdS/*i*-ZnO/ZnO:Al/Al, prepared as described above. Capacitance-Voltage measurements were carried out using an Agilent 4294A precision impedance analyzer. The frequency varied from 1 kHz to 1 MHz, and temperature swept from 315K to 15K. DC bias voltage swept from 1.0V reverse bias to 0.2V forward bias.¹⁹ DLT spectra were measured using a commercial DLTS system that used Fourier transforms to characterize the transients at a reverse bias voltage (V_R) of -2 V, a trap-filling pulse (V_P) of 0 V, and saturation pulse widths (t_P) of 10 μs and 100 ms.²⁰

The commonly used supercell approach²¹ was used to explore the defect physics in CuSbS₂. The first-principles calculations were performed with the Vienna ab initio simulation package (VASP),^{22,23} using the projected augmented wave (PAW) method^{24,25} implemented therein. The standard Perdew-Burke-Ernzerhof (PBE) generalized gradient approximation to the exchange correlation was chosen,²⁶ and an on-site Hubbard $U=5$ eV was applied to the Cu d orbitals to reduce the self-interaction-error.²⁷ A 96-atom supercell was used to model the defect systems, with the lattice vectors fixed to the pure phase. The errors related to the finite supercell size, band gap error, and elemental reference energy were corrected according to prior literature reports.^{28,29}

3. Results and discussion

The pre- and post-thermally treated films (pre-TT and TT-11h, respectively), as well as the crystals, are phase-pure orthorhombic CuSbS₂, as shown in the x-ray diffraction (XRD) patterns in Figure S1, Supplementary Information. Based on XRF characterization, we also

conclude that the thermal treatment does not change the stoichiometry or thickness of the films. Crystals, pre-TT and TT-11h films maintain a slightly Cu-poor composition with a ratio of $\text{Cu}/(\text{Cu}+\text{Sb})=0.48$, within the error of the XRF measurement compared to the nominal CuSbS_2 stoichiometry. The Hall effect shows that the hole concentrations of the pre-TT and TT-11h films are mid- 10^{16} and 10^{17} cm^{-3} , respectively. However, PV devices made with the TT-11h films surprisingly show only a slight increase in the efficiency comparing to the one made with non-annealed films, while the significant improvements in the morphology and optoelectronic properties due to the thermal treatment⁷ would suggest a much better performance in the TT-11h device. This unexpected behavior encouraged us to find the defects that may limit the device performance.

3.1 Admittance- and deep-level transient spectroscopies

To characterize the TT-11h film by AS and DTLS, devices of the $\text{Mo}/p\text{-CuSbS}_2/n\text{-CdS}/i\text{-ZnO}/\text{ZnO:Al}/\text{Al}$ architecture were made, as previously described.^{7,17,18} From AS (Fig. 1A), we observed the presence of the three electronic defects: a shallow one at about 0.08 eV, and two deeper ones at 0.17 eV and 0.24 eV above the valence band maximum. The corresponding densities of defect states are $10^{15} \text{ cm}^{-1}\text{eV}^{-1}$ and $10^{16} \text{ cm}^{-1}\text{eV}^{-1}$. The Arrhenius plot for the more abundant deeper defect showed a slope of -0.24 eV, corresponding to its activation energy (Fig. 1A, inset). Previous defect calculations³ suggest the shallow transition at 0.08 eV to be associated with copper vacancy (V_{Cu}), but experimental support for this assignment is needed. Regardless, this shallow defect is unlikely the limiting factor to the CuSbS_2 solar-cell device performance. Instead, the two transitions close to 0.2 eV related to deeper defects may be more detrimental.

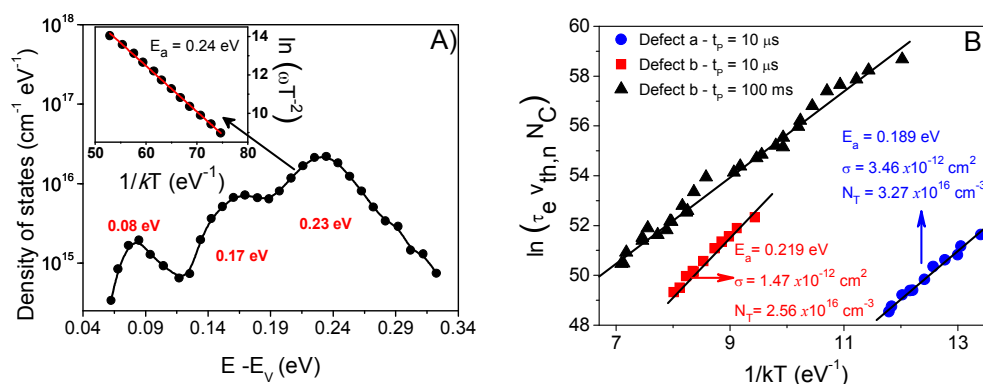


Fig. 1 A) Density of defects states versus energy obtained from the admittance spectroscopy. Inset shows the Arrhenius plot for the peak at about 0.23 eV. B) Arrhenius plot from DLTS measurements at saturation pulses width (t_p) of 10 μ s and 100 ms. The values of activation energy (E_a), capture cross-section (σ) and effective density of traps states (N_T) for each defect is also shown.

To study the two deeper defects, we performed temperature-dependent DLTS, with the results shown in Fig. 1B for two different saturation pulse widths (t_p) of 10 μ s and 100 ms. The activation energies of the deeper defects are approximately 0.19 and 0.22 eV from the short 10 ms saturation DLTS, similar to those from the 100 ms saturation result (Fig. 1B inset), and close to the results obtained by AS. From the sign of the DLTS signal (not shown here), we could also conclude that these deep defects are hole traps (acceptors). The capture cross-section (σ) and effective density of trapping states (N_T) for each defect were determined to be $1.5\text{--}3.5 \times 10^{-12}$ cm² and of $2.6\text{--}3.3 \times 10^{16}$ cm⁻³, the latter of which are in reasonable agreement with the results from AS. These results are similar to those in CIGS,²¹ and can be used for future CuSbS₂ photovoltaic device performance simulations.

3.2 Photoluminescence spectroscopy

The results of AS and DLTS measurements together indicate that there are both shallow and deep defects that may influence the performance of the PV devices with thermally treated CuSbS₂ absorbers. For more information about the microscopic origin of these defects, three

types of CuSbS_2 films with different preparation conditions were characterized: as-deposited films, thermally treated films, and the microcrystals. For each sample, we performed photoluminescence spectroscopy measurements, evaluating the temperature and the excitation power dependencies of the radiative defects signatures.

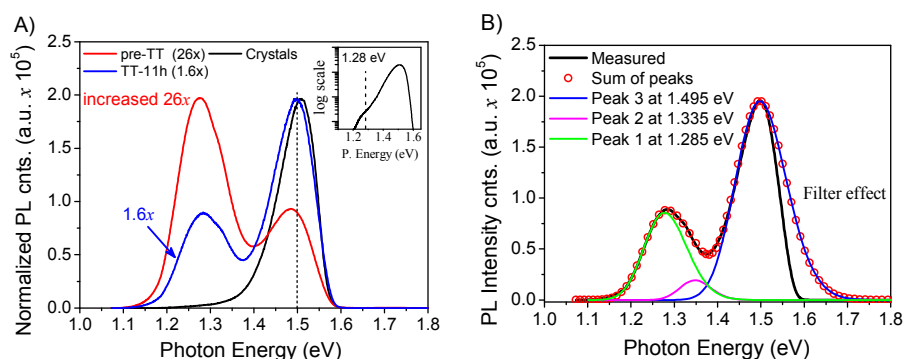


Fig. 2 A) Normalized PL spectra of the crystals, pre-TT (increased 26x) and TT-11h (increased 1.6x) films at 4.25 K and laser power of 2.2 mW. Insert shows the crystals spectrum in logarithmic scale. B) Deconvolution of the TT-11h PL spectrum (increased 1.6x). The asymmetric shape observed for the peak 3 was caused by filter cut-off.

Figure 2 shows the normalized PL spectra at 4.25 K and the laser power of 2.2 mW for the three samples (Fig. 2A) and the de-convolution of the TT-11h PL spectrum (Fig. 2B). The film samples show two visible peaks at about 1.29 and 1.50 eV, with a little shoulder at about 1.34 eV. Meanwhile, the crystals show a peak around 1.50 eV, with a negligible contribution of the peak at about 1.29 eV (insert in Figure 2A). Since the wide peak around 1.29 eV has an evident shoulder at about 1.34 eV (Fig. 1A), the PL spectra were deconvoluted for estimating the position and intensity of each contribution. As shown in Figure 2B, the PL spectra of the CuSbS_2 films are deconvoluted into three Gaussians-like peaks at about 1.29 eV (peak 1), 1.34 eV (peak 2), and 1.50 eV (peak 3). Since the CuSbS_2 band gap at 4.25 K is 1.58 eV,³⁰ these peaks (1, 2 and 3) are ~ 0.29 , ~ 0.24 and ~ 0.08 eV

below the band-gap. These energies from PL of the CuSbS₂ materials (Fig. 2b) agree reasonably well with those from AS and DLTS of the CuSbS₂ devices (Fig. 1). We conclude that they originate from the same defects.

Since the de-convolution of peaks 1 and 2 is not unambiguous enough, we subsequently analyze them together (peak 1+2). Comparing the spectra of different thin-film samples in Figure 2A, we find that the TT-11h film has a higher ratio between the peaks 3 and 1+2 and also a 16-time higher intensity for peak 3 than the pre-TT film. This means that the annealed film has a lower concentration of defects associated with the peak 1+2 and less non-radiative centers. The fact of the peak 1+2 decreases and almost disappears when the material goes from pre-TT through TT-11h to crystals, makes us believe that the associated defects are progressively eliminated with the increase of the sulfur and antimony chemical potentials, promoted by thermal treatment in Sb₂S₃ vapor. This observation suggests that the chemical origin of these defects is related to Sb and S deficiency in the as-deposited CuSbS₂ thin-film sample.

3.3 Power-Dependent Photoluminescence

Figure 3 shows the integrated PL intensity of the peak 3 (left side) and of the sum of the peaks 1 and 2 (right side) as a function of the excitation laser power, along with the power law fit of the data. The integrated PL intensity can be fitted by the following power law:³¹

$$I_{\text{PL}} \propto P^{\gamma} \quad (1),$$

where I_{PL} is the integrated PL intensity and P is the excitation laser power. The dimensionless exponent γ is known to be $1 < \gamma < 2$ for free-exciton or bound-exciton recombination, and $\gamma < 1$ for free-to-bound (FB) or donor-acceptor pair (DAP) recombination luminescence.³¹ The spectra at different laser powers for the crystals and TT-11h films can be seen in Figure S2, Supplementary Information.

In Figure 3, all peaks show $\gamma < 1$, and hence these processes can be associated with FB or DAP recombination. For DAP recombination, the energy of the peaks should shift significantly as the laser power increases.^{8,9} As shown in the derivative of intensity as a function of energy (Figure S2), the peak shift is < 4 meV/dec for peak 3 and < 2 meV/dec for peak 1+2, indicating that these processes cannot be related to DAP recombination; thus, they may be related to the FB recombination. This low peak shift also indicates that potential defects that are known to be deleterious for the solar cell performance^{32–34} are small in CuSbS₂.

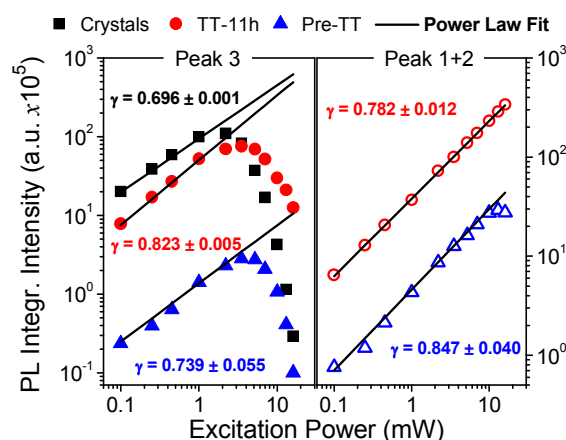


Fig. 3 PL integrated intensity as a function of excitation power for peak 3 (filled symbols, left side) and the sum of peaks 1 and 2 (unfilled symbols, right side). Black squares, blue triangles, and red circles represent the crystals, pre-TT and TT-11h films, respectively. The solid line is the power law fit, following Eq. 1.

In addition to the power law dependence at low excitation powers, a sharp decrease of peak 3 intensity is observed at an excitation power higher than 2.2 mW (left side of Figure 3). The quenching behavior of peak 3 is not observed for the peak 1+2. We relate this quenching behavior to the local heating up of the samples at a high laser excitation: since peak 3 can be associated with a very shallow trap with a relatively low density (Fig. 1A), a small elevation of temperature can promote the thermal activation of this defect. Supporting this hypothesis, the crystals show a more abrupt quenching behavior, because thermal dissipation is harder in

the isolated thicker (~ 3 to $5\ \mu\text{m}$ tall) crystals than in the uniform films (thickness of $\sim 1.5\ \mu\text{m}$). The surface and cross-section SEM images of these films can be seen in Figure S3 in Supplementary Material. A similar PL quenching behavior has been also observed in $\text{Cu}_2\text{ZnSnS}_4$ polycrystals.³⁵

3.4 Temperature-Dependent Photoluminescence

Figures 4A and Figure 4B show the temperature dependent PL intensity of peak 3 and peak 1+2, respectively. The PL intensity dependence as a function of the temperature for a free-to-bound recombination can be fitted using the following equation,^{9,36,37}

$$I_{\text{FB}}(T) = \frac{A T^{-\alpha}}{1 + (N_{\text{v}}^*/p) T^{3/2} \exp(-E_{\text{a}}/kT)} \quad (2),$$

where A is a constant, $N_{\text{v}}^* = 2(2\pi m_{\text{h}} k/h^2)^{3/2}$ is the density of states, m_{h} is the hole effective mass, h is the Planck constant, p is the hole concentration, E_{a} is the ionization energy (activation energy), k is the Boltzmann constant, and T is the absolute temperature. The PL spectrum dependence on temperature for TT-11h film is shown in Figure S4 in Supplementary Material.

From these results, one can conclude that for all samples the PL peaks show the common quenching behavior as the temperature increases (or kT^{-1} decreases). This trend can be associated with the thermal dissociation of the respective radiative centers, and with the increase of non-radiative recombination. We also observe a small increase in the PL emission intensity for peak 1+2 at $(kT)^{-1} \sim 0.5 \times 10^3\ \text{eV}^{-1}$ with an increasing temperature. This phenomenon is due to the redistribution of the carriers with the quenching of peak 3.³⁸ From Figure 4, we note that the PL integrated intensity has a low rate of quenching at the low-temperature region, whereas above 19 K (for the peak 3) and 40 K (for the peaks 1 and 2), it

decreases abruptly with increasing temperature. Peak 3 is totally quenched at about 40 K for all films, while the peak 1+2 thermalizes around 140 K and 230 K for pre-TT and TT-11h, respectively.

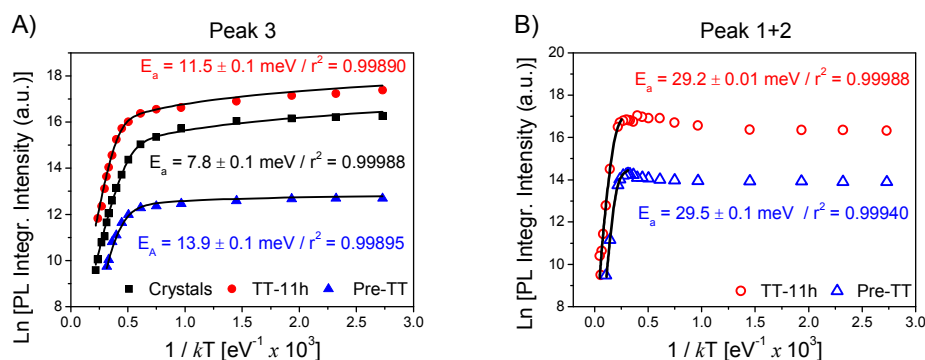


Fig. 4 PL integrated intensity versus $(kT)^{-1}$ for A) peak 3 (filled symbols) and B) sum of the peaks 1 and 2 (unfilled symbols). Squares, triangles, and circles symbols are for crystals, pre-TT and TT-11h films, respectively. The full line represents the Arrhenius fit, following Eq. 2.

The defect ionization energies E_a , and the ratio of the density of states to the hole concentration N_v^*/p can be estimated from the fitting of the Figure 4 data using Eq.(2). The exponent “ α ” can be deduced from the low-temperature region, where the exponential term can be neglected so that $\log(I_{\text{FB}}(T))$ becomes linear to $-\alpha \log(T)$ (the hole concentration can be assumed constant at the temperature range of fitting). The straight line region at low temperature for the relation $\log(I_{\text{FB}}(T))$ versus $\log(T)$ for all peaks and samples show a slope of 0.33, leading to the E_a and N_v^*/p values summarized in Table 1. The E_a for peak 1+2 of the films was around 29 meV, close to the 22.9-24.8 meV value observed for an acceptor level in Cu_2SnS_3 .³¹ The presence of defects/peak 1+2 also has a slight effect on the stability of the defect/peak 3, with E_a ranging from 7.85 to 13.95 meV.

Table 1 Values of ionization energy (E_a) and density of state/hole concentration (N_v/p) for defects states associated with peak 3 and to peak 1+2. These values were obtained from Eq. 2 fitting of the experimental data shown in Fig. 4.

Sample	Peak 3		Peak 1+2	
	E_a (meV)	N_v / p	E_a (meV)	N_v / p
Crystals	7.85 ± 0.12	0.80 ± 0.06	---	---
Pre-TT	13.95 ± 0.09	2.62 ± 0.10	29.49 ± 0.12	1.85 ± 0.04
TT-11h	11.55 ± 0.09	1.24 ± 0.05	29.24 ± 0.01	0.88 ± 0.01

Comparing the pre-exponential factor N_v/p of the two types of thin films presented in Table 1, we conclude that the hole concentration in the TT-11h film is about two times higher than in the pre-TT film. This agrees with our Hall effect measurement⁶ of 10^{17} cm^{-3} and mid- 10^{16} cm^{-3} in the TT-11h film and in the pre-TT film, respectively. With these hole concentrations and the N_v/p results in Table 1, we can estimate the hole effective mass by $N_v^* = 2(2\pi m_h k/h^2)^{3/2}$. For the TT-11h films we estimate $m_h = 6.9 - 8.7 m_0$, and for Pre-TT film we estimate $m_h = 3.9 - 4.9 m_0$, where m_0 is a mass of free electron. These values are ~ 10 times heavier than for CIGS,³⁹ in good agreement with the theoretical calculations.³⁰

3.5 Band-to-band recombination

An interesting PL phenomenon observed at the higher temperature range (from 110 K to room temperature) deserves more attention. Specifically, we observed the appearance of a new peak (referred to as NP below) with energy close to the band gap. The energies of different peaks as a function of temperature, in comparison with the temperature dependence of the indirect band gap determined from optical absorption measurements⁴⁰ are shown in Fig. 5. The PL spectra as a function of temperature in this 110 – 300K range is given in

Figure S4B of Supplementary Material. The temperature dependence of the peaks energy and band gap were fitted using the following empiric equation proposed by Varshni:⁴¹

$$E(T) = E_0 - AT^2/(B + T) \quad (3),$$

where A and B are empirical constants and E_0 is the energy gap at 0 K.

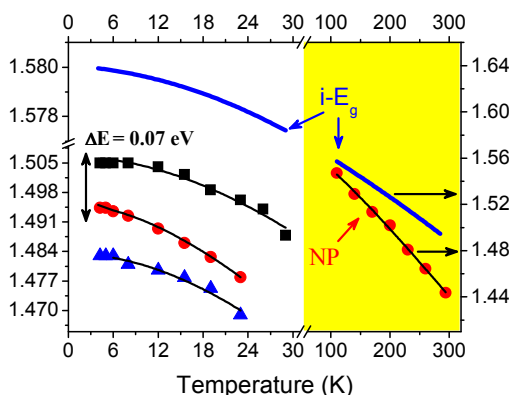


Fig. 5 Temperature dependence of the peak energy for peak 3 and NP. Squares, triangles, and circles symbols are for crystals, pre-TT and TT-11h films, respectively. The bold blue line represent the temperature dependence of the indirect band gap ($i-E_g$) of the TT-11h film.⁴⁰ The full line represents the Varshni fit, following empiric Eq. 3.

The best Varshni fit of the experimental data shown in Figure 5 is achieved with the parameters summarized in Table 2. Since E_0 for the NP peak is equal to the observed E_0 for the indirect band gap, it is likely that this radiative process is due to a band-to-band recombination (BB). The occurrence of BB at high temperatures in polycrystalline materials is not uncommon. For example, it has been also observed in kesterites (such as CZTS³⁵) and chalcopyrite (such as AgGaTe₂⁴²). However, the appearance of the band-to-band recombination is quite remarkable for the CuSbS₂ material, since indirect-gap semiconductors usually show overall weak PL. From Table 2, we also observe that the crystals show a higher E_0 for peak 3, consistent with the lower ionization energy of the acceptor defect associated with this transition.

Table 2 Varshni empirical constants obtained from Eq. 3 fit of the experimental data shown in Fig. 5.

Sample	A (meV K ⁻¹)	B (K)	E ₀ (eV)	E ₀ (i-E _g) – E ₀ (eV)
Indirect band-gap (i-E _g) TT-11h ⁴⁰	0.411	106	1.580	0.000
Crystals (peak 3)	0.414	179	1.506	0.074
Pre-TT (peak 3)	0.517	179	1.483	0.097
TT-11h (peak 3)	0.461	179	1.495	0.085
TT-11h (NP)	0.655	122	1.580	0.000

3.6 Defect theoretical calculations

The above analysis of the temperature- and power-dependent PL measurements for different CuSbS₂ samples provides additional insights into the characteristics of the defects observed in CuSbS₂ photovoltaic devices. For example, it is clear now that the deeper defects responsible for PL and AS/DLTS signals in as-deposited samples are related to the Sb- and/or S-deficiency. To identify the likely atomic-scale origin of these defects, we performed calculation of the formation enthalpy of different possible point defects that can be present in CuSbS₂ under the experimental S- and Sb-rich and Cu-poor processing conditions that correspond to thermal treatments.

The calculated room temperature hole concentration as a function of growth temperature (Fig. 6A) and the corresponding defect formation enthalpies as a function of Fermi level (Fig. 6B) are shown in Fig.6. According to Figure 6A, at the S-rich, Cu-poor, and Sb-rich condition, the calculated hole concentration (10^{16} - 10^{17} cm⁻³) agree well with the results of the Hall effect measurements. The plot of defect formation energies (Fig. 6B) confirms that the most abundant acceptor at the experimental Cu-poor (S-rich, Sb-rich) conditions is copper vacancy (V_{Cu}). The V_{Cu} transition level (-/0) is very shallow, ~ 0.03 eV above the valence band maximum (VBM), in agreement with previous calculations of CuSbS₂³ and also with CuSbSe₂ calculation results.⁶ Copper on antimony antisite (Cu_{Sb}) is also an active acceptor defect, but with a higher formation energy and deeper transition levels

(0.15 and 0.25 eV). The presence of V_{Sb} should be very rare, because its formation enthalpy (ΔH_f) is 2-3 eV higher than V_{Cu} and Cu_{Sb} under the *p*-type condition.

The dominant donor defects are Cu interstitials (Cu_i). We have considered two different interstitial sites, one within the layer (Cu_{i-in}), and another one between the layers (Cu_{i-out}). Both of them are shallow donor defects (transition levels close to conduction band minimum), with the latter having slightly higher formation energy. The sulfur vacancies (V_{S-in} and V_{S-out}) also have relatively low ΔH_f . These vacancies have amphoteric character, acting as a donor or an acceptor depending on the position of the Fermi level (E_F). The (0/+) transition level is around 0.15 eV for V_{S-out} and 0.35 eV for V_{S-in} , and the (2+/+) transition level is around 0.10 eV for V_{S-out} .

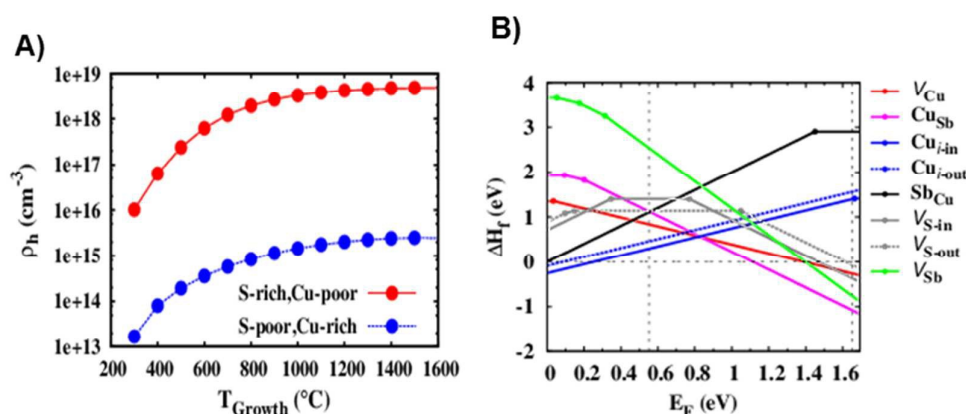


Fig. 6 Calculated (A) hole concentration at different synthesis conditions as a function of growth temperature, and (B) defect formation energies as a function of Fermi level (E_F)

According to the results of our calculations, the position of the Fermi level in $CuSbS_2$ is determined by Cu_i donors and V_{Cu} acceptors. The equilibrium between these two defects sets the Fermi level (E_F) position around 0.8 eV during the thermal treatment, where they intercept in Fig. 6B. It is important to note that at this E_F position, the formation enthalpy of the Cu_{Sb} and V_S defects are also comparable to that of V_{Cu} and Cu_i , so Cu_{Sb} and V_S may be

present in substantial quantities. At room temperature, the equilibrium Fermi level drops to 0.5 – 0.6 eV above the valence band maximum.

Based on these theoretical results, we propose that the deep acceptor signatures experimentally observed in the PL, AS and C-DLTS measurements results from Cu_{Sb} and/or V_{S} defects. This conclusion is consistent with the observation that the PL signatures of these defects are progressively eliminated with the increase of the sulfur and antimony chemical potentials, promoted by thermal treatment in Sb_2S_3 vapor. Such proposed model for deep defects does not exclude the presence of Cu_{i} defects in CuSbS_2 . It is likely that this shallow defect was completely ionized at all studied temperatures and saturation pulses widths, making their experimental observations difficult.

4. Summary and conclusions

The results of different experimental measurements (PL, AS, DLTS) and theoretical calculations are summarized in the hypothetical CuSbS_2 defects diagram in Figure 7. Based on this diagram we can also propose a simplistic mechanism that explains the appearing of the band-to-band (BB) recombination at increased measurement temperature. The increase in temperature makes the neutral acceptor defects associated with the free-to-bound (FB) radiative channels thermally dissociate, donating holes to the valence band. In other words, as these acceptor defects become occupied by electrons that are thermally excited from the valence band, the photoexcited electrons in the valence band lose the ability to recombine through the corresponding free-to-bound (FB) radiative channels, and the BB radiative channel becomes progressively dominant. Figure 7 shows this phenomenon as a function of temperature, taking as an example the experimental behavior of the TT-11h film. It is also worth mentioning that CuSbS_2 has a slightly indirect band-gap, which makes the phonon-assisted BB recombination have higher probability with increasing temperature.

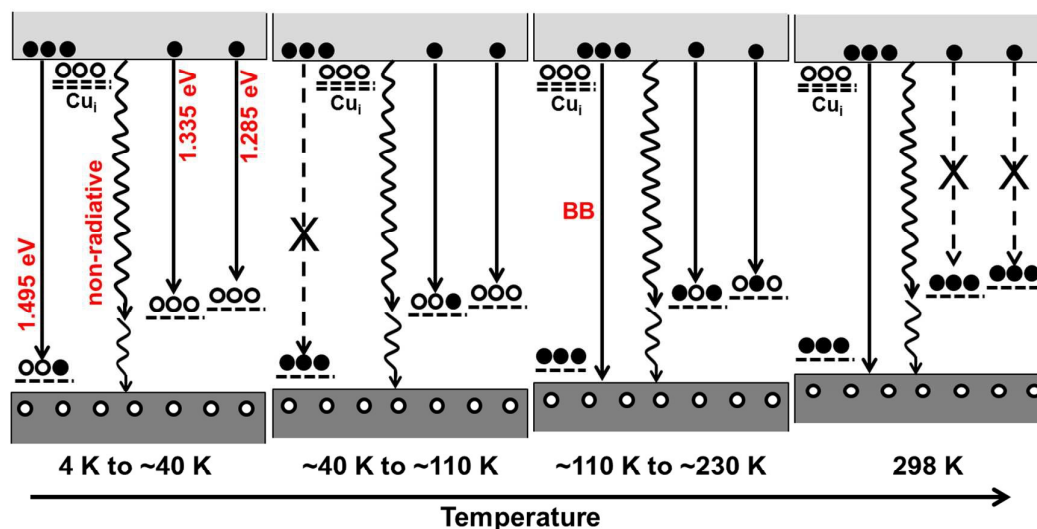


Fig. 7 Schematic energy diagram for the photoluminescence transitions observed for TT-11h CuSbS₂ film at different temperature ranges. The upper light gray and bottom dark gray rectangles represent the conduction and the valence bands, and the filled and unfilled circles represent the electrons and holes, respectively. The solid and dashed black arrows symbolize the active and quenched radiative recombinations respectively, while the waved arrows are the non-radiative transitions.

In conclusion, we experimentally characterized different defects present in CuSbS₂ and, identified their likely atomic origins with aid of theoretical calculation. The AS, DLTS and PL results show three acceptor defects: a shallow one at about 0.08 eV and two deeper ones at 0.17 eV and 0.24 eV above the valence band. Based on the results of the theoretical calculation, we propose that the defects at 0.08 eV are associated with V_{Cu}, the ones at 0.17 eV and 0.24 eV are related to V_S and/or Cu_{Sb} acceptors. From the experimental results, we also estimated the acceptor densities of $\sim 10^{16} \text{ cm}^{-3}$, capture cross-section σ of $\sim 10^{-12} \text{ cm}^2$, and hole effective masses of $\sim 6.1 m_0$, which can be used for CuSbS₂ photovoltaic device simulations. Overall, these results provide new insights into CuSbS₂ defects, which can aid with future improvement in solar cells based on this emerging photovoltaic absorber.

Acknowledgements

This work was supported by the U. S. Department of Energy, Office of Energy Efficiency and Renewable Energy, Solar Energy Technology Program, under Contract No. DE-AC36-08GO28308 to NREL. For the execution of this work, F.W.S.L was funded by the São Paulo Research Foundation (FAPESP), grant 2014/12166-3 and grant 2016/10513-3. We would like to thank Lauryn Baranowski and Adam Welch for providing as-deposited CuSbS₂ samples and for useful technical discussions.

References

1. A. W. Welch, P. P. Zawadzki, S. Lany, C. A. Wolden and A. Zakutayev, *Sol. Energy Mater. Sol. Cells*, 2015, **132**, 499–506.
2. B. Krishnan, S. Shaji and R. Ernesto Ornelas, *J. Mater. Sci. Mater. Electron.*, 2015, **26**, 4770–4781.
3. B. Yang, L. Wang, J. Han, Y. Zhou, H. Song, S. Chen, J. Zhong, L. Lv, D. Niu and J. Tang, *Chem. Mater.*, 2014, **26**, 3135–3143.
4. W. Septina, S. Ikeda, Y. Iga, T. Harada and M. Matsumura, *Thin Solid Films*, 2014, **550**, 700–704.
5. L. Shi, Y. Li, C. Wu and Y. Dai, *J. Alloys Compd.*, 2015, **648**, 507–511.
6. A. W. Welch, L. L. Baranowski, P. Zawadzki, S. Lany, C. A. Wolden and A. Zakutayev, *Appl. Phys. Express*, 2015, **8**, 82301.
7. F. W. de Souza Lucas, A. W. Welch, L. L. Baranowski, P. C. Dippo, H. Hempel, T. Unold, R. Eichberger, B. Blank, U. Rau, L. H. Mascaro and A. Zakutayev, *J. Phys. Chem. C*, 2016, **120**, 18377–18385.
8. M. A. Reshchikov and H. Morkoç, *J. Appl. Phys.*, 2005, **97**, 61301.
9. S. Levchenko, V. E. Tezlevan, E. Arushanov, S. Schorr and T. Unold, *Phys. Rev. B*, 2012, **86**, 45206.
10. J. Vidal, S. Lany, M. D’Avezac, A. Zunger, A. Zakutayev, J. Francis and J. Tate, *Appl. Phys. Lett.*, 2012, **100**, 32104.
11. A. Zakutayev, C. M. Caskey, A. N. Fioretti, D. S. Ginley, J. Vidal, V. Stevanovic, E. Tea and S. Lany, *J. Phys. Chem. Lett.*, 2014, **5**, 1117–1125.
12. A. Zakutayev, X. Zhang, A. Nagaraja, L. Yu, S. Lany, T. O. Mason, D. S. Ginley and A. Zunger, *J. Am. Chem. Soc.*, 2013, **135**, 10048–10054.
13. L. L. Baranowski, K. McLaughlin, P. Zawadzki, S. Lany, A. Norman, H. Hempel, R. Eichberger, T. Unold, E. S. Toberer and A. Zakutayev, *Phys. Rev. Appl.*, 2015, **4**, 44017.
14. L. L. Baranowski, P. Zawadzki, S. Lany, E. S. Toberer and A. Zakutayev, *Semicond.*

- Sci. Technol.*, 2016, **31**, 123004.
15. S. Das, S. K. Chaudhuri, R. N. Bhattacharya and K. C. Mandal, *Appl. Phys. Lett.*, 2014, **104**, 192106.
 16. A. W. Welch, L. L. Baranowski, F. W. de Souza Lucas, E. S. Toberer, C. A. Wolden and A. Zakutayev, in *2015 IEEE 42nd Photovoltaic Specialist Conference (PVSC)*, IEEE, 2015, pp. 1–4.
 17. F. W. de Souza Lucas, A. W. Welch, L. L. Baranowski, P. C. Dippo, L. H. Mascaro and A. Zakutayev, in *2015 IEEE 42nd Photovoltaic Specialist Conference (PVSC)*, IEEE, 2015, pp. 1–5.
 18. M. A. Contreras, M. J. Romero, B. To, F. Hasoon, R. Noufi, S. Ward and K. Ramanathan, *Thin Solid Films*, 2002, **403–404**, 204–211.
 19. T. Walter, R. Herberholz, C. Müller and H. W. Schock, *J. Appl. Phys.*, 1996, **80**, 4411.
 20. S. Weiss and R. Kassing, *Solid. State. Electron.*, 1988, **31**, 1733–1742.
 21. C. Freysoldt, B. Grabowski, T. Hickel, J. Neugebauer, G. Kresse, A. Janotti and C. G. Van de Walle, *Rev. Mod. Phys.*, 2014, **86**, 253–305.
 22. G. Kresse and J. Furthmüller, *Phys. Rev. B*, 1996, **54**, 11169–11186.
 23. G. Kresse and J. Hafner, *Phys. Rev. B*, 1994, **49**, 14251–14269.
 24. P. E. Blöchl, *Phys. Rev. B*, 1994, **50**, 17953–17979.
 25. G. Kresse and D. Joubert, *Phys. Rev. B*, 1999, **59**, 1758–1775.
 26. J. P. Perdew, K. Burke and M. Ernzerhof, *Phys. Rev. Lett.*, 1996, **77**, 3865–3868.
 27. S. L. Dudarev, G. A. Botton, S. Y. Savrasov, C. J. Humphreys and A. P. Sutton, *Phys. Rev. B*, 1998, **57**, 1505–1509.
 28. H. Peng, D. O. Scanlon, V. Stevanovic, J. Vidal, G. W. Watson and S. Lany, *Phys. Rev. B*, 2013, **88**, 115201.
 29. S. Lany and A. Zunger, *Phys. Rev. B*, 2008, **78**, 235104.
 30. D. J. Temple, A. B. Kehoe, J. P. Allen, G. W. Watson and D. O. Scanlon, *J. Phys. Chem. C*, 2012, **116**, 7334–7340.
 31. N. Aihara, K. Tanaka, H. Uchiki, A. Kanai and H. Araki, *Appl. Phys. Lett.*, 2015, **107**, 32101.
 32. D. P. Halliday, R. Claridge, M. C. J. Goodman, B. G. Mendis, K. Durose and J. D. Major, *J. Appl. Phys.*, 2013, **113**, 223503.
 33. J. P. Leitão, N. M. Santos, P. A. Fernandes, P. M. P. Salomé, A. F. da Cunha, J. C. González, G. M. Ribeiro and F. M. Matinaga, *Phys. Rev. B*, 2011, **84**, 24120.
 34. L. Van Puyvelde, J. Lauwaert, P. F. Smet, S. Khelifi, T. Ericson, J. J. Scragg, D. Poelman, R. Van Deun, C. Platzer-Björkman and H. Vrielinck, *Thin Solid Films*, 2015, **582**, 146–150.
 35. M. Grossberg, P. Salu, J. Raudoja and J. Krustok, *J. Photonics Energy*, 2013, **3**, 30599.
 36. K. Maeda, *J. Phys. Chem. Solids*, 1965, **26**, 595–605.
 37. J. J. Krustok, H. Collan and K. Hjelt, *J. Appl. Phys.*, 1997, **81**, 1442.
 38. A. Aydinli, N. M. Gasanly and K. Göksen, *J. Appl. Phys.*, 2000, **88**, 7144–7149.
 39. I. Repins, S. Glynn, J. Duenow, T. J. Coutts, W. K. Metzger and M. A. Contreras,

- Proc. SPIE 7409, Thin Film Solar Technology*, 2009, 74090M; doi:10.1117/12.828365.
40. M. Birkett, PhD. Thesis, University of Liverpool, 2016.
41. E. G. Seebauer and M. C. Kratzer, *Charged Semiconductor Defects*, Springer London, London, 2009.
42. J. Krustok, A. Jagomagi, M. Grossberg, J. Raudoja and M. Danilson, *Sol. Energy Mater. Sol. Cells*, 2006, **90**, 1973–1982.